www.sciencemag.org/content/362/6418/1040/suppl/DC1

Supplementary Material for

Uniaxial pressure control of competing orders in a high-temperature superconductor

H.-H. Kim, S. M. Souliou, M. E. Barber, E. Lefrançois, M. Minola, M. Tortora, R. Heid, N. Nandi, R. A. Borzi, G. Garbarino, A. Bosak, J. Porras, T. Loew, M. König, P. M. Moll, A. P. Mackenzie, B. Keimer, C. W. Hicks, M. Le Tacon*

*Corresponding author. Email: matthieu.letacon@kit.edu

Published 30 November 2018, *Science* **362**, 1040 (2017)
DOI: 10.1126/science.aat4708

This PDF file includes:

Materials and Methods

Single crystals of $YBa_2Cu_3O_{6+x}$ were grown using a flux method (*48*), and the oxygen content was adjusted to x~0.67 (T_c = 65 K) by annealing under well-defined oxygen partial pressure. The sample was mechanically detwinned by heating under uniaxial stress (50-60MPa was applied at 400 °C). The untwinned nature of the sample was checked using a polarized microscope and further confirmed by x-ray diffraction.

When preparing samples for IXS experiments under uniaxial strain, several requirements have to be met:

i) The sample has to be prepared as a beam, where stress is applied along the beam's length.

ii) To avoid large elastic scattering coming from the Ortho-VIII oxygen order superstructures, the sample should be mounted for access to the (0 k l) scattering plane.

iii) To maximize the scattering signal from the sample, it is preferable to have a sample thickness of ~ 40 μm along the beam direction (comparable to the absorption length of the incident x-rays).

To this aim, the crystals were cut and manually polished to needles of dimension 2.6mm x 0.15mm x 0.2mm (a x b x c). The center of the sample was further thinned down along the b-direction (normal to the surface) using a xenon plasma focused ion beam (PFIB). A PFIB mills much faster than a gallium-based focused ion beam, and any implanted xenon diffuses out of the sample without reacting chemically. This sample form allows high strains to be achieved in the centre, "necked" part of the sample, while allowing thicker end portions that act as handles for convenient mounting in the uniaxial stress apparatus, and in which the stress is lower. The necked part is ~200 μm long and has a final thickness of ~40 μm.

Strain device

The strain device utilized in this experiment is a modified version of the device used in refs. *(31-33)*. It has been specially designed to allow working in transmission, with access to a large region of reciprocal space. For this, the cell is provided with an aperture with a wide angular opening (±45 degrees) for the transmitted photons (Fig. S1). To carry out temperature-dependent measurements, the device has been adapted to fit into a He-flow cryostat used at the European Synchrotron Radiation Facility that is built to accept pressure cells. Our strain device is symmetric, so that the sample is centered on the axis of rotation of this cryostat. The cell is held by a special holder designed to minimize the possible thermal stress on the device. The temperature was measured by placing a silicon diode sensor on the device. The lowest temperature reached in this experiment was T=15K.

Inelastic X-ray scattering under Uniaxial Strain

Inelastic X-ray scattering (IXS) experiments were performed at the beamline ID-28 of the European Synchrotron Radiation Facility (ESRF). The incident energy was tuned to 17.794 keV using the (9 9 9) Bragg peak of the silicon crystal monochromator. This gives an energy resolution of ~3 meV (see below). The size of the incident beam on the sample is 50 x 40 μm, which is smaller than the central necked region of the sample. The scattered photons were analyzed by 9 crystal analyzers placed at the end of a 7-m long arm. The entrance slits of the analyzers were set to 20 mm in the scattering plane and 55 mm perpendicular to the plane. This gives a corresponding momentum resolution (FWHM) of $\Delta k = 0.004$ (r.l.u.), $\Delta l = 0.05$ (r.l.u.).

Supplementary Text

Strain Control and Estimation

Strain is applied to the sample by applying voltages to the piezoelectric stacks. Sensors based on parallel-plate capacitors, indicated in Fig. S1 are used to measure the displacement that is applied to the sample and the sample plates. As can be seen in the photograph in Fig. 1 of the main text, and schematically in Fig. S1, the plates that hold the sample give some flexibility: the sample is held by relatively thin bars, labelled "flexible bars" in the figure, that flex as stress is applied to the sample. The plates were designed in this way to reduce the risk of inadvertent thermal displacements breaking the sample during cooling. The thin bars protect the sample by reducing the efficiency with which displacements generated by the piezoelectric actuators are transmitted to the sample. It is an acceptable trade-off because the necked portion of the sample is short: The actuators can apply a displacement of up to ~30 μm, which would, if transmitted with perfect efficiency to the 0.3 mm-long necked portion of the sample, result in a strain of ~10%, which is well above the maximum target strain for this experiment.

During measurement, the displacement applied to the plates and sample (d), and so also the sample strain, was held constant using a feedback loop on the displacement sensors. To obtain the conversion constant between the measured capacitance and sample strain, nuclear Bragg reflections were monitored. Only a few Bragg reflections could be conveniently accessed; Fig. S2 shows our measurement of the (0 0 6) Bragg peak at a series of applied strains. As compressive strain is applied, the (0 0 6) Bragg peak shows a systematic shift towards smaller 2θ, corresponding to the extension of the c-axis lattice parameter associated with compression along the a-axis. The Bragg peak does not broaden by more than 10% as strain is applied, which shows that the strain is homogeneous in the probed volume of the sample. Prior to the IXS experiments, we measured the *ac* and *bc* Poisson's ratio of our single crystal at the high-pressure diffraction beamline ID-27 of ESRF, obtaining the value $\nu_{ac} \sim \nu_{bc} = 0.25 \pm 0.02$ (Fig. S3).

In Fig. S3 we plot $-\varepsilon_{xx} = \varepsilon_{zz}/\nu_{ac}$ versus the applied displacement d, where ε_{zz} is the c-axis strain derived from the location of the (0 0 6) nuclear Bragg peak. Identifying d=0 is always a slightly subtle issue; here, we took a reading from the displacement sensor at room temperature with no voltage on the actuators, and then adjusted the voltage on the actuators while cooling to keep the sensor reading constant. The flexibility of the sample plates reduces the effect of differential thermal contraction between the cell and sample, so this procedure should bring the sample to well within 0.1% strain of its true neutral strain point.

At low strains, $-\varepsilon_{xx}$ is proportional to d, as expected. At large applied displacements, $-\varepsilon_{zz}/\nu_{ac}$ appears to saturate. One possible interpretation is that the epoxy holding the sample started to rupture, reducing the stress achieved in the sample for a given applied displacement. However, none of the data from the sample presented in the main text, nor the T_c measurements to be presented shortly, saturate at high strains. Nor was any hysteresis observed: normally, epoxy rupture or damage to the sample results in strong hysteresis in measurements. Therefore, we conclude that deformation of the sample and epoxy remained elastic over our entire strain range, with ε_{xx} proportional to applied displacement. Whether the apparent saturation of the applied strain arises from a nonlinear relationship between ε_{zz} and ε_{xx} at large strains, or something more mundane such as bending of the sample at high strains, remains to be determined.

At this stage, we obtain our conversion between d and ε_{xx} from a linear fit to the low-strain data, shown in Fig. S4, yielding a maximal applied strain of ~1 ±0.2 %. The error bar reflects the

uncertainty on the actual strain value and is estimated on the basis of the observed decrease of the critical temperature (see below measurement of T_c) and of the evolution of the c-axis lattice parameter.

Analysis and elastic line subtraction

To allow accurate subtraction of the elastic lines, especially close to the strong long-range CDW superstructure peaks, it is crucial to measure precisely the actual energy resolution function. This was determined from inelastic scattering measurements on a piece of PMMA, in experimental conditions similar to those of our experiment. The best fit to the measured resolution function was obtained using a Pseudo-Voigt profile:

$$PV(x) = A\left(m \times \frac{2}{\pi} \frac{w_L}{4x^2 + {w_L}^2} + (1 - m) \times \sqrt{\frac{4\ln 2}{\pi}} \frac{e^{-4ln(2)x^2/{w_G}^2}}{w_G} \right)$$

Where w_L and w_G are respective Lorentzian and Gaussian linewidths of the resolution function and m the Lorentz factor. Typical resolution close to Q_{CDW} is shown in Fig. S5, for which the fitting parameters are:

$$w_L = 3{,}32\ meV$$
$$w_G = 2{,}71\ meV$$
$$m = 0{,}62$$

The IXS spectra were fitted using a sum of a resolution limited elastic line and of Lorentzian lines (convoluted with the resolution function) at finite frequency for the phonons. Examples of such fitting are shown in Fig. S5**.**

The inelastic part of the spectra shown in the Fig. 4 of the manuscript were obtained by subtracting the elastic line extracted from this fitting procedure (never before). Importantly, all features presented in the Fig. 4 (in particular the soft phonon mode) can already be clearly distinguished in the raw data, as illustrated in Fig. S6, where we show the raw IXS data at -1.0% compression at T = 41 K and T = 70K.

Error bars on the parameters shown in the figures of the paper are defined as the standard error from the Levenberg-Marquardt fitting procedure. In some cases where unphysically small errors have been obtained, fitting accuracy was tested by forcing one parameter (e.g. mode energy) to a different value and monitoring degradation of the fit quality (through the reduced-χ^2 and convergence criteria).

T_c measurements

In this Supplemental Information, we report two measurements of T_c versus *a*-axis strain of $YBa_2Cu_3O_{6+x}$. The first is on a sample with a zero-stress T_c of $T_{c,0} \approx 59$ K, and in a configuration optimized for measurement of T_c. The second is on the sample described in the main text, which was probed by inelastic x-ray scattering, and which had $T_{c,0} \approx 65$ K.

The 59 K sample was polished by hand to a uniform thickness. In order to probe only a small sample volume, so as to reduce the effects of possible large-scale inhomogeneity, a

microfabricated sensor was used. The sensor consisted of a GaAs/AlGaAs 2DEG hall cross, 4 μm across, and a 20 μm-diameter excitation coil deposited around it (Fig. S7). The hall cross measures the field generated with the excitation coil. When the sensor is placed on the sample, the onset of superconductivity is visible as a reduction in the measured field, due to the Meissner screening of the sample. Measurements were performed at frequencies between 0.1 and 10 kHz, and with excitation fields between 0.5 and 3 Oe, oriented predominantly along the sample's *c* axis. As seen in Fig. S7A, the width of the superconducting transition hardly changed with applied strain, indicating a highly homogeneous strain field within the probed volume.

We take T_c to be the temperature where$|d\chi/dT|$ is maximum. As shown in Fig. S7B, T_c decreases, with increasing slope, with *a*-axis compression. No hysteresis was observed between increasing- and decreasing-strain ramps, indicating that the sample and epoxy deformation was elastic over this strain range. Previous thermal expansion measurements on a sample with similar doping found the slope dT_c/dp_a, evaluated at zero pressure, to be -1.5 K/GPa (29). Converting our strain dependence to the same units, using the elastic tensor reported in Ref. (49), we find $dT_c/dp_a = -1.8$ K/GPa at zero pressure. Within the error on our determination of the sample strain, this value agrees with the result from the thermal expansion measurement.

The sample and mounting geometry of the IXS sample did not allow use of the same hall cross susceptometer. Therefore, to determine its T_c, two three-turn coils were wound from 15 μm-diameter copper wire around the central portion of the sample, which was thinned using a plasma focused ion beam, and their mutual inductance was measured. This measurement was performed after the IXS measurements, in a different cryostat. Excitation fields of between 0.01 and 1 Oe were used, at frequencies between 0.1 and 100 kHz. The excitation field was oriented predominantly along the sample's *a* axis. During measurement, the sample was found to have been cracked, such that it could be compressed but not tensioned. We identify the zero-strain point as the point where T_c starts to change with applied displacement.

The raw data are shown in Fig. S8. The coils could not be wound tightly around the sample without risk of damage to the sample, and therefore they probe a much larger volume of the sample than the x-ray beam in the IXS measurements. They probe not only the central thinned portion of the sample, but also the thicker "roots", where the strain will be lower than in the thinned portion. Therefore, in the raw data the transition becomes broad as strain is applied. However, the thinned portion of the sample experiences the highest strain and should, therefore, show the strongest response. It is clear that T_c decreases, with increasing slope, with *a*-axis compression, and we estimate T_c = 48 ± 5 K at $\varepsilon_{xx} \sim -1\%$.

First Principle calculations

The density-functional calculations shown in the main text were carried out for a fully oxygenated $YBa_2Cu_3O_7$ using the mixed-basis pseudopotential method (50,51). The electron-ion interaction was represented by norm-conserving pseudopotentials, and we included the semi-core states Y-4s, Y-4*p*, Ba-5*s*, Ba-5*p*, and O-2*s* in the valence space. In the mixed-basis approach valence states are expanded in a basis set consisting of a combination of plane waves and local functions. The latter allow an efficient description of the most localized components of the valence states. In particular, we used plane waves up to a kinetic energy of 20 Ry, augmented by local functions of *s*,*p*,i type at the Y and Ba sites, of *s* and *p* type at the O sites, and of *d* type at the Cu sites. For the exchange-correlation functional, we employed the local-density approximation (52), and Brillouin

zone integrations were performed with a 12x12x4 orthorhombic *k*-point grid in conjunction with a Gaussian smearing of 0.2 eV. Further details can be found in Ref. (53). Lattice dynamics properties were calculated using the linear response or density-functional perturbation theory implemented in the mixed-basis scheme (54). Dynamical matrices were first calculated on a 4x4x2 orthorhombic grid and then obtained for arbitrary points in the Brillouin zone by standard Fourier-interpolation technique, which entered the calculation of the phonon dispersion and structure factors. To estimate the effect of strain on the phonon spectrum, we performed calculations for two geometries. The unstrained case was represented by full optimization of the orthorhombic structure. In the second geometry we simulated a compressive strain along the *a*-axis, $\varepsilon_{xx} = \delta a/a = -1\%$, and considered the other two axes elongated, assuming a Poisson ratio of 0.25 ($\delta b/b = \delta c/c = 0.25\%$). An optimization of the atomic positions was performed for this distorted orthorhombic unit cell. The corresponding phonon dispersions along (010) for the two relevant representations Δ'_1 and Δ'_4, shown in Fig. S9 indicate a negligible effect of strain on the modes below 15 meV.

Calculated IXS intensity

The general form of $S(\boldsymbol{Q},\omega)$ for single-phonon scattering takes the following form (55):

$$S(\boldsymbol{Q},\omega) = \sum_j G(\boldsymbol{Q},j)F(\boldsymbol{Q},\omega,T,j)$$

where

$$G(\boldsymbol{Q},j) = \left|\sum_d f_d(\boldsymbol{Q})e^{-W_d(\boldsymbol{Q})+i\boldsymbol{Q}.\boldsymbol{r_d}}\left(\boldsymbol{Q}.\hat{\boldsymbol{\sigma}}_d^j(\boldsymbol{q})\right)M_d^{-1/2}\right|^2$$

and the thermal factor can be written as

$$F(\boldsymbol{Q},\omega,T,j) = \frac{1}{\omega}\left[(\langle n(\omega,T)\rangle + 1)\delta\big(\omega - \omega(j,\boldsymbol{Q})\big) + \langle n(\omega,T)\rangle\delta\big(\omega + \omega(j,\boldsymbol{Q})\big)\right]$$

with the thermal occupation (Bose) factor is given by $\langle n(\omega,T)\rangle = \frac{1}{e^{\omega/k_BT}-1}$, $\omega(j,\boldsymbol{Q})$ is the energy of mode *j* at momentum transfer $\boldsymbol{Q}$, f_d is the atomic scattering factor of atom *d* (here we neglected the $\boldsymbol{Q}$ dependence of this quantity to evaluate the scattering intensity and simply used $f_d(\boldsymbol{Q}) = \sqrt{Z_d}, Z_d$ being the atomic number of atom *d*) with mass M_d, $W_d(\boldsymbol{Q})$ the Debye-Waller factor at the position $\boldsymbol{r_d}$, $\hat{\boldsymbol{\sigma}}_d^j(\boldsymbol{q})$ is the *d*-site projected component of 3*N*-dimensional normalized eigenvector of the phonon mode *j* defined in periodic notations $\hat{\boldsymbol{\sigma}}_d^j(\boldsymbol{q}+\boldsymbol{\tau}) = \hat{\boldsymbol{\sigma}}_d^j(\boldsymbol{q})$, where $\boldsymbol{\tau}$ is an arbitrary reciprocal lattice vector and $\boldsymbol{q} = \boldsymbol{Q} - \boldsymbol{\tau}$ is the reduced momentum transfer.

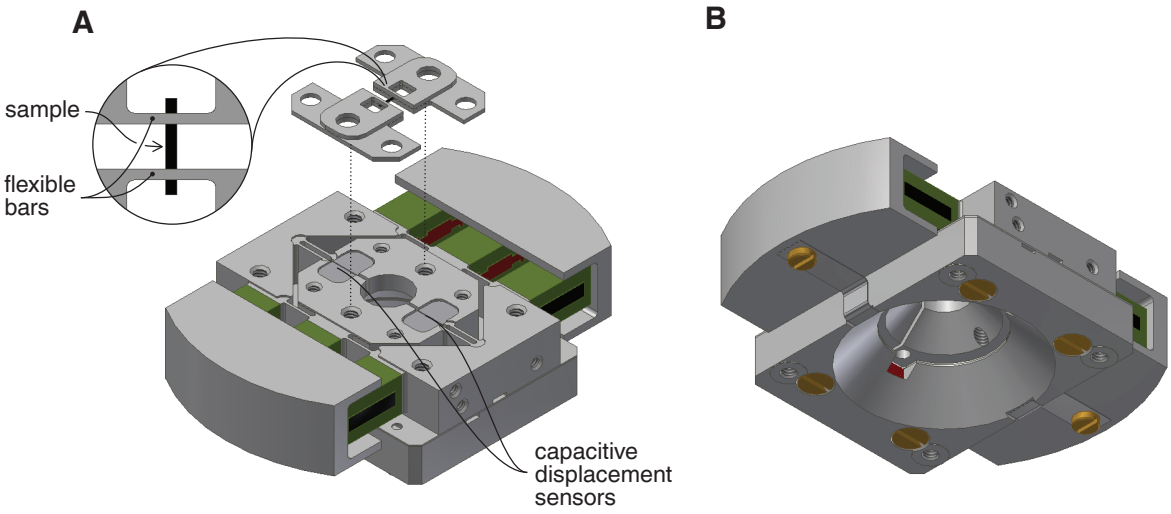

Fig. S1. Strain device for the inelastic x-ray scattering experiment. A- Sample side. B- back side, with large opening.

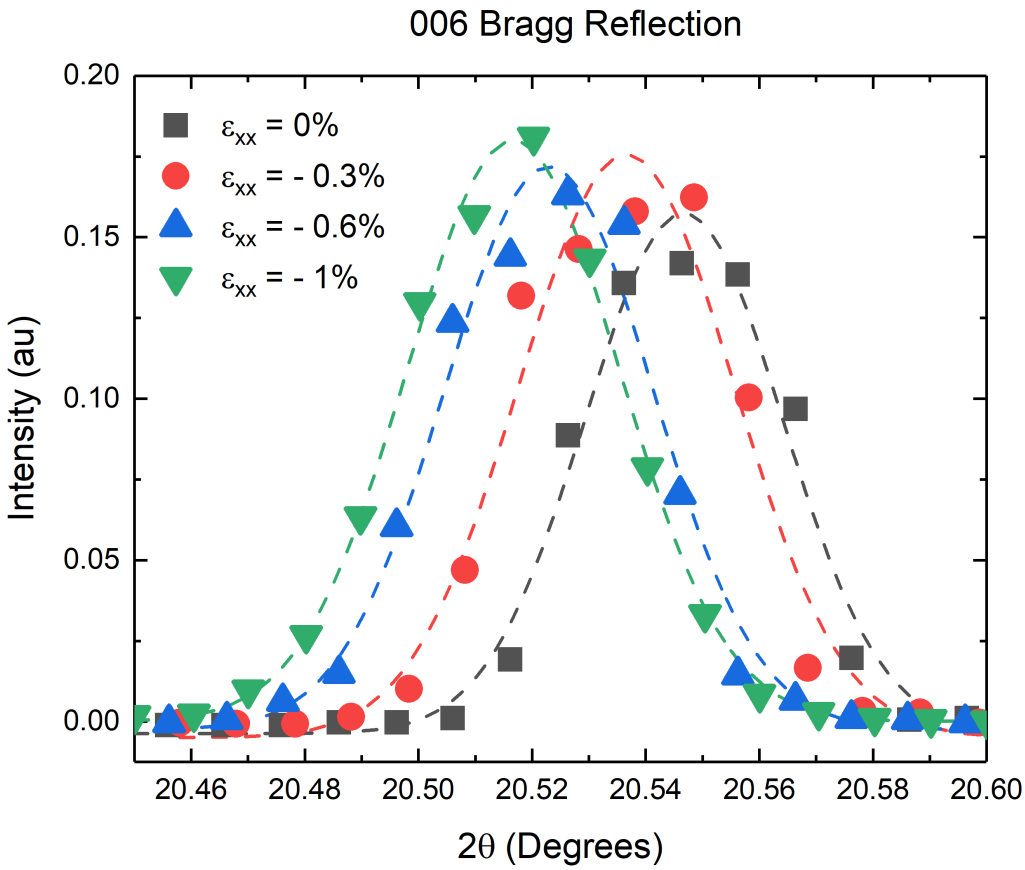

Fig. S2. (0 0 6) Bragg Peak (measured from the IXS spectrometer) as a function of the estimated applied strain (see text). Dashed lines are Gaussian fits to the data.

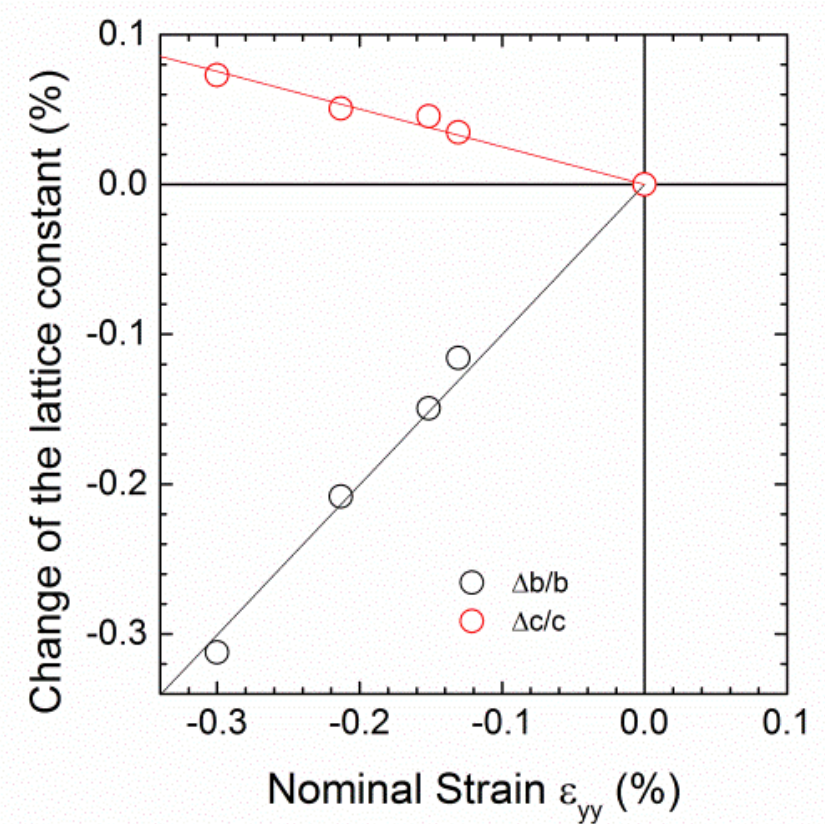

Fig. S3. Change of the b and c lattice constants (measured from diffraction) against nominal strain (estimated from the capacitance sensor) along b-direction. Measured at T = 55 K.

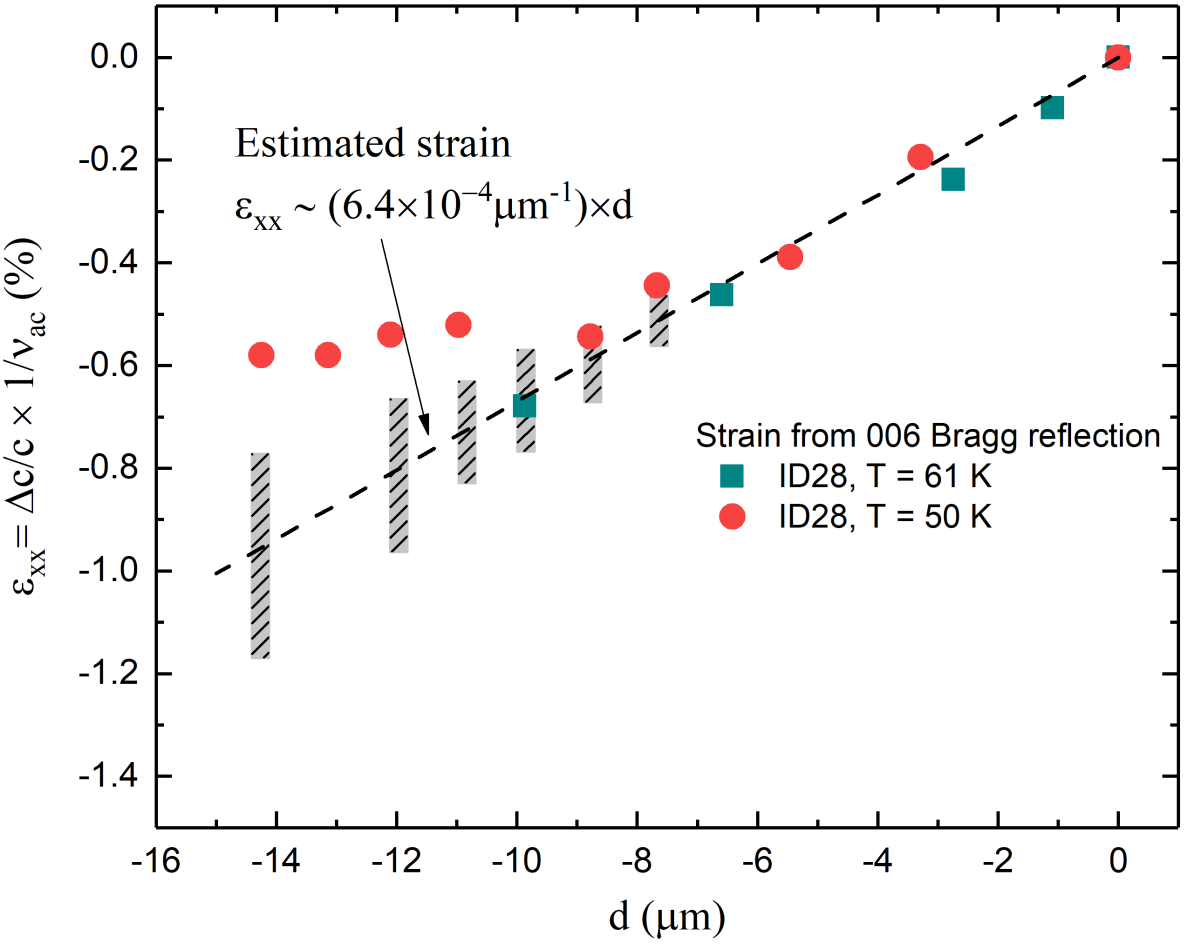

Fig. S4. Estimated *a*-axis strain, based on the location of the (0 0 6) nuclear Bragg peak, versus applied displacement *d*. As explained in the text, our strain estimate is based on a linear fitting to the data at low strain (The shaded grey areas at high strain represent error bars – see text).

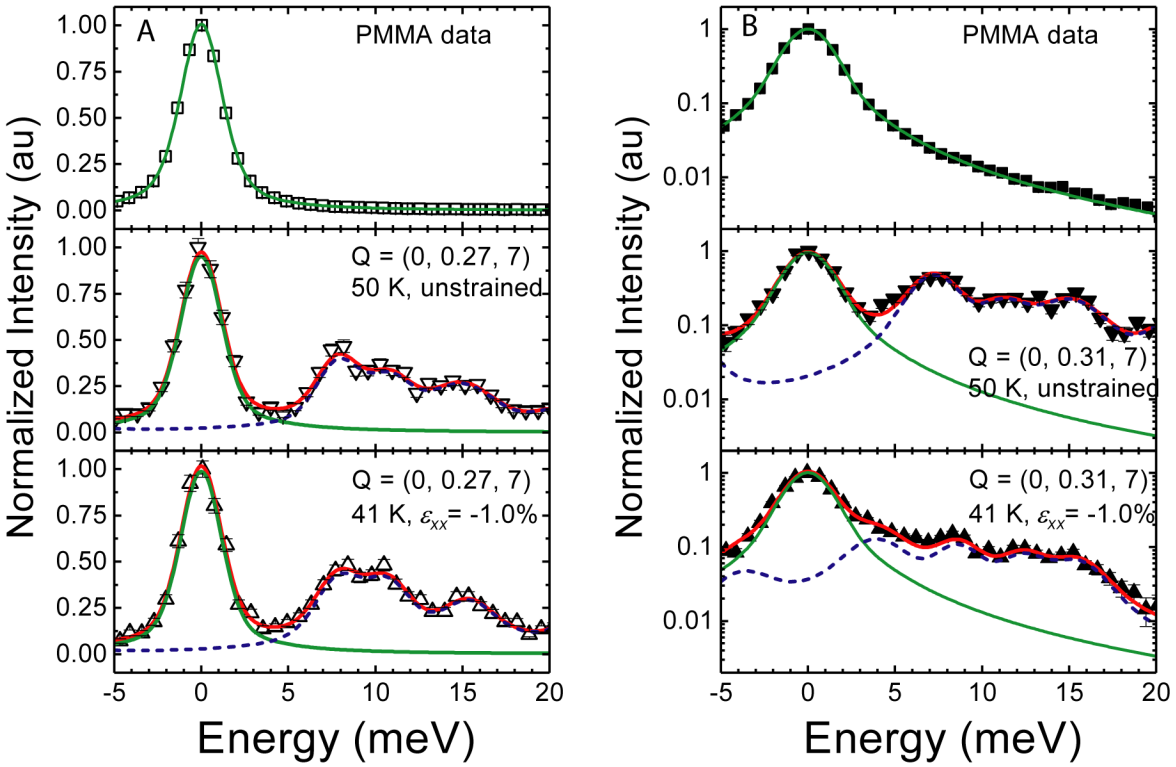

Fig. S5. A. (top) Determination of the resolution function (the green line is a fit to a Pseudo-voigt profile). Detail of the fit of an IXS spectra at Q = (0, 0.27, 7) at unstrained (middle) and strained (bottom) cases. B. (top) Determination of the resolution function, now plotted in logarithmic scale. Details of the fit of an IXS spectra close to Q_{3D} = (0, 0.31, 7) at unstrained (middle) and (bottom) strained conditions. The extra contribution of the soft mode in the tail of the large CDW elastic line is evident.

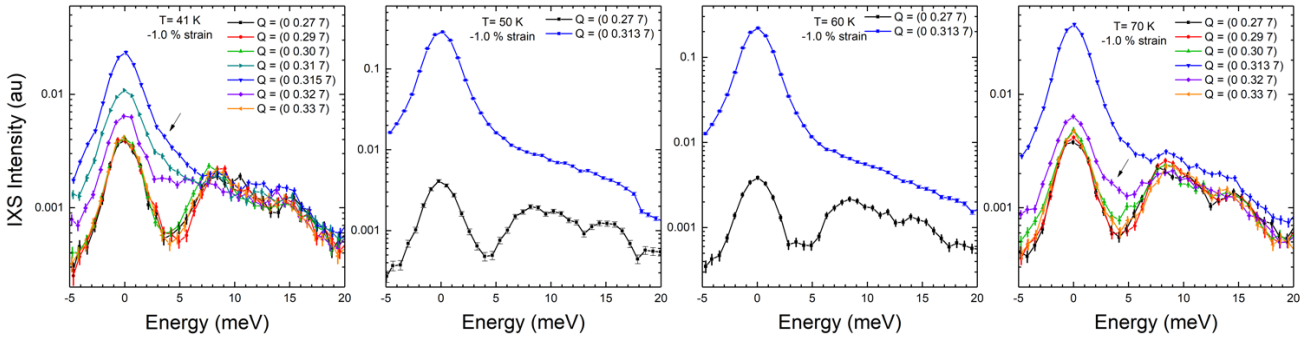

Fig. S6. Raw IXS data at 41, 50, 60 and 70 K across Q_{3D} under the highest compression ($\boldsymbol{\varepsilon_{xx}\sim -1.0}$%). This clearly shows a soft inelastic feature a low frequency at 41 K and 70 K (indicated by the arrow). At Q_{3D}, no phonons can be distinguished from the very strong elastic line at 50 K and 60 K.

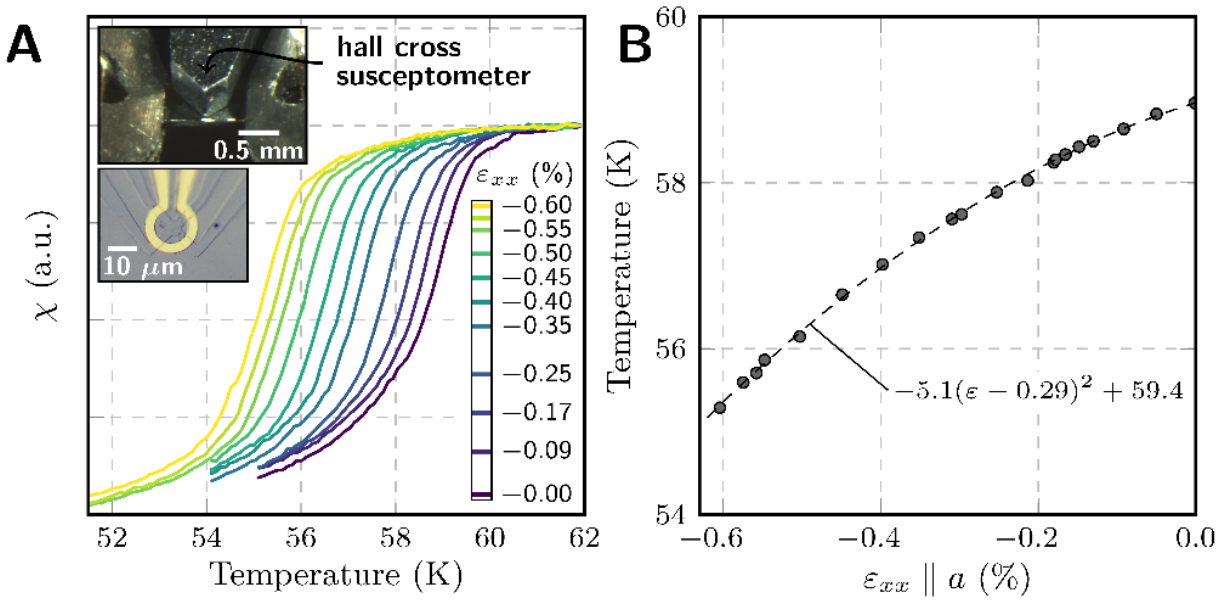

Fig. S7. $\boldsymbol{T_c}$ versus strain of a hand-polished sample. A. ac magnetic susceptibility versus temperature at various applied strains $\boldsymbol{\varepsilon_{xx}}$. The sensor and its placement on top of the sample are shown in the insets. The signal from the hall cross was found to drift over time, so the curves are all scaled to the same value at 62 K. B. $\boldsymbol{T_c}$ versus strain determined from the data in panel A, taking $\boldsymbol{T_c}$ as the point with maximum $\boldsymbol{|d\chi/dT|}$.

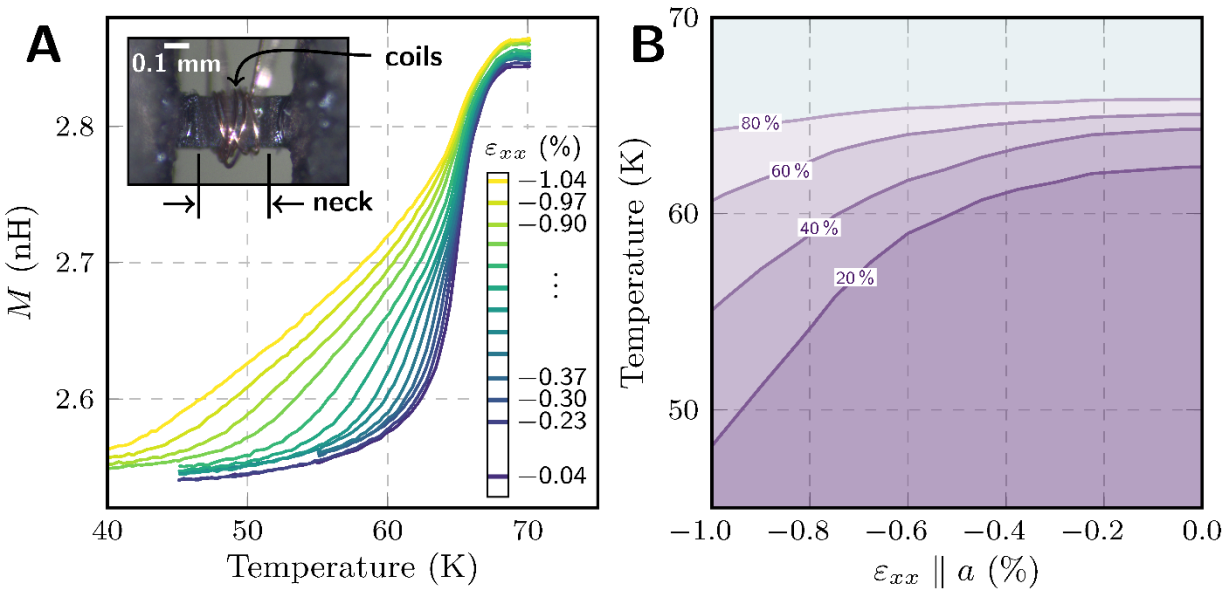

Fig. S8. $\boldsymbol{T_c}$ versus strain of the sample probed by IXS. A. Mutual inductance of two coils wrapped around the thinned portion of the sample. Because the coils also pick up some of the thicker portion of the sample, the measured transition becomes broad as pressure is applied. B. Cuts through the data of panel A at constant mutual inductance levels (2.60, 2.66, 2.72, and 2.78 nH), illustrating the downward trend in $\boldsymbol{T_c}$ with *a*-axis compression.

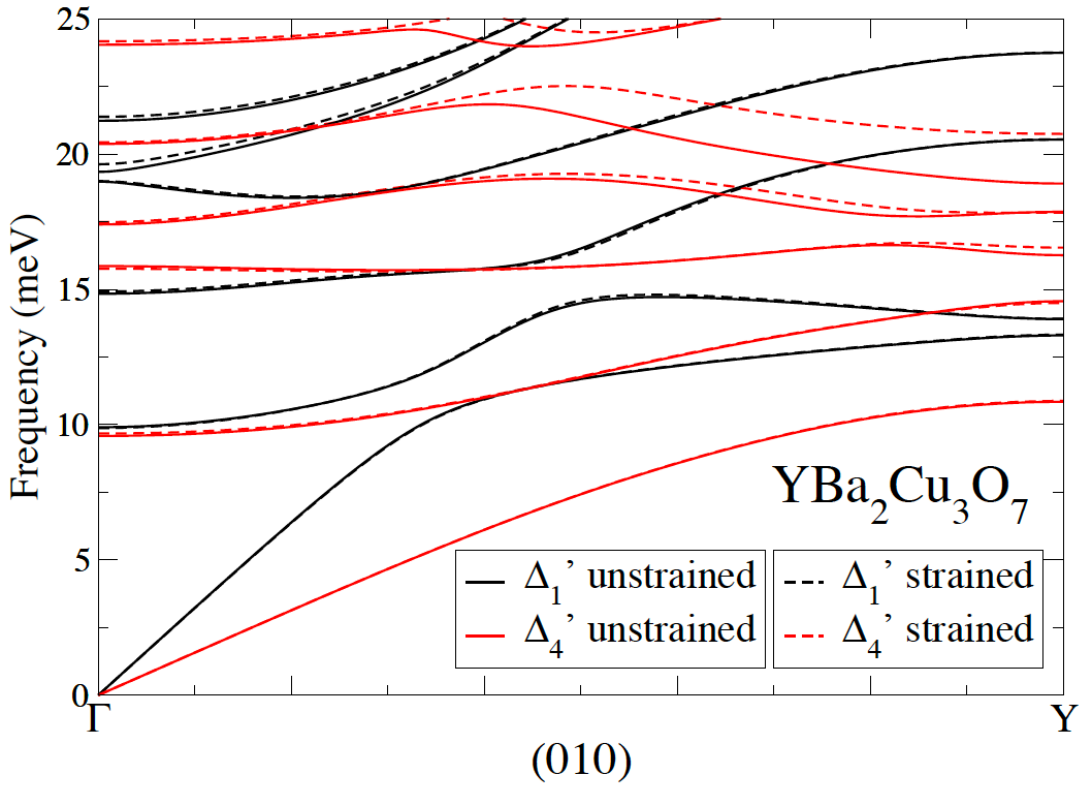

Fig. S9. Strain effect on the low energy part of the $\mathbf{\Delta'_1}$ and $\mathbf{\Delta'_4}$ phonon branches.

References and Notes

1. B. Keimer, S. A. Kivelson, M. R. Norman, S. Uchida, J. Zaanen, From quantum matter to high-temperature superconductivity in copper oxides. *Nature* **518**, 179–186 (2015). doi:10.1038/nature14165 Medline

2. J. M. Tranquada, B. J. Sternlieb, J. D. Axe, Y. Nakamura, S. Uchida, Evidence for stripe correlations of spins and holes in copper oxide superconductors. *Nature* **375**, 561–563 (1995). doi:10.1038/375561a0

3. M. Vojta, Lattice symmetry breaking in cuprate superconductors: Stripes, nematics, and superconductivity. *Adv. Phys.* **58**, 699–820 (2009). doi:10.1080/00018730903122242

4. J. E. Hoffman, E. W. Hudson, K. M. Lang, V. Madhavan, H. Eisaki, S. Uchida, J. C. Davis, A four unit cell periodic pattern of quasi-particle states surrounding vortex cores in $Bi_2Sr_2CaCu_2O_{8+\delta}$. *Science* **295**, 466–469 (2002). doi:10.1126/science.1066974 Medline

5. C. Howald, H. Eisaki, N. Kaneko, M. Greven, A. Kapitulnik, Periodic density-of-states modulations in superconducting $Bi_2Sr_2CaCu_2O_{8+\delta}$. *Phys. Rev. B* **67**, 014533 (2003). doi:10.1103/PhysRevB.67.014533

6. W. D. Wise, M. C. Boyer, K. Chatterjee, T. Kondo, T. Takeuchi, H. Ikuta, Y. Wang, E. W. Hudson, Charge-density-wave origin of cuprate checkerboard visualized by scanning tunnelling microscopy. *Nat. Phys.* **4**, 696–699 (2008). doi:10.1038/nphys1021

7. G. Ghiringhelli, M. Le Tacon, M. Minola, S. Blanco-Canosa, C. Mazzoli, N. B. Brookes, G. M. De Luca, A. Frano, D. G. Hawthorn, F. He, T. Loew, M. Moretti Sala, D. C. Peets, M. Salluzzo, E. Schierle, R. Sutarto, G. A. Sawatzky, E. Weschke, B. Keimer, L. Braicovich, Long-range incommensurate charge fluctuations in $(Y,Nd)Ba_2Cu_3O_{(6+x)}$. *Science* **337**, 821–825 (2012). doi:10.1126/science.1223532 Medline

8. J. Chang, E. Blackburn, A. T. Holmes, N. B. Christensen, J. Larsen, J. Mesot, R. Liang, D. A. Bonn, W. N. Hardy, A. Watenphul, M. Zimmermann, E. M. Forgan, S. M. Hayden, Direct observation of competition between superconductivity and charge density wave order in $YBa_2Cu_3O_{6.67}$. *Nat. Phys.* **8**, 871–876 (2012). doi:10.1038/nphys2456

9. S. Blanco-Canosa, A. Frano, T. Loew, Y. Lu, J. Porras, G. Ghiringhelli, M. Minola, C. Mazzoli, L. Braicovich, E. Schierle, E. Weschke, M. Le Tacon, B. Keimer, Momentum-dependent charge correlations in $YBa_2Cu_3O_{6+\delta}$ superconductors probed by resonant x-ray scattering: Evidence for three competing phases. *Phys. Rev. Lett.* **110**, 187001 (2013). doi:10.1103/PhysRevLett.110.187001 Medline

10. T. P. Croft, C. Lester, M. S. Senn, A. Bombardi, S. M. Hayden, Charge density wave fluctuations in $La_{2-x}Sr_xCuO_4$ and their competition with superconductivity. *Phys. Rev. B* **89**, 224513 (2014). doi:10.1103/PhysRevB.89.224513

11. E. H. da Silva Neto, B. Yu, M. Minola, R. Sutarto, E. Schierle, F. Boschini, M. Zonno, M. Bluschke, J. Higgins, Y. Li, G. Yu, E. Weschke, F. He, M. Le Tacon, R. L. Greene, M. Greven, G. A. Sawatzky, B. Keimer, A. Damascelli, Doping-dependent charge order correlations in electron-doped cuprates. *Sci. Adv.* **2**, e1600782 (2016). doi:10.1126/sciadv.1600782 Medline

12. W. Tabis, B. Yu, I. Bialo, M. Bluschke, T. Kolodziej, A. Kozlowski, E. Blackburn, K. Sen, E. M. Forgan, M. Zimmermann, Y. Tang, E. Weschke, B. Vignolle, M. Hepting, H. Gretarsson, R. Sutarto, F. He, M. Le Tacon, N. Barišić, G. Yu, M. Greven, Synchrotron x-ray scattering study of charge-density-wave order in $HgBa_2CuO_{4+\delta}$. *Phys. Rev. B* **96**, 134510 (2017). doi:10.1103/PhysRevB.96.134510

13. A. Perali, C. Castellani, C. Di Castro, M. Grilli, *d*-wave superconductivity near charge instabilities. *Phys. Rev. B Condens. Matter* **54**, 16216–16225 (1996). doi:10.1103/PhysRevB.54.16216 Medline

14. S. A. Kivelson, E. Fradkin, V. J. Emery, Electronic liquid-crystal phases of a doped Mott insulator. *Nature* **393**, 550–553 (1998). doi:10.1038/31177

15. L. E. Hayward, D. G. Hawthorn, R. G. Melko, S. Sachdev, Angular fluctuations of a multicomponent order describe the pseudogap of $YBa_2Cu_3O_{(6+x)}$. *Science* **343**, 1336–1339 (2014). doi:10.1126/science.1246310 Medline

16. T. Wu, H. Mayaffre, S. Krämer, M. Horvatić, C. Berthier, W. N. Hardy, R. Liang, D. A. Bonn, M.-H. Julien, Incipient charge order observed by NMR in the normal state of YBa2Cu3Oy. *Nat. Commun.* **6**, 6438 (2015). doi:10.1038/ncomms7438 Medline

17. S. Gerber, H. Jang, H. Nojiri, S. Matsuzawa, H. Yasumura, D. A. Bonn, R. Liang, W. N. Hardy, Z. Islam, A. Mehta, S. Song, M. Sikorski, D. Stefanescu, Y. Feng, S. A. Kivelson, T. P. Devereaux, Z.-X. Shen, C.-C. Kao, W.-S. Lee, D. Zhu, J.-S. Lee, Three-dimensional charge density wave order in $YBa_2Cu_3O_{6.67}$ at high magnetic fields. *Science* **350**, 949–952 (2015). doi:10.1126/science.aac6257 Medline

18. H. Jang, W.-S. Lee, H. Nojiri, S. Matsuzawa, H. Yasumura, L. Nie, A. V. Maharaj, S. Gerber, Y.-J. Liu, A. Mehta, D. A. Bonn, R. Liang, W. N. Hardy, C. A. Burns, Z. Islam, S. Song, J. Hastings, T. P. Devereaux, Z.-X. Shen, S. A. Kivelson, C.-C. Kao, D. Zhu, J.-S. Lee, Ideal charge-density-wave order in the high-field state of superconducting YBCO. *Proc. Natl. Acad. Sci. U.S.A.* **113**, 14645–14650 (2016). doi:10.1073/pnas.1612849113 Medline

19. J. Chang, E. Blackburn, O. Ivashko, A. T. Holmes, N. B. Christensen, M. Hücker, R. Liang, D. A. Bonn, W. N. Hardy, U. Rütt, M. V. Zimmermann, E. M. Forgan, S. M. Hayden, Magnetic field controlled charge density wave coupling in underdoped $YBa_2Cu_3O_{6+x}$. *Nat. Commun.* **7**, 11494 (2016). doi:10.1038/ncomms11494 Medline

20. F. Yu, M. Hirschberger, T. Loew, G. Li, B. J. Lawson, T. Asaba, J. B. Kemper, T. Liang, J. Porras, G. S. Boebinger, J. Singleton, B. Keimer, L. Li, N. P. Ong, Magnetic phase diagram of underdoped $YBa_2Cu_3O_y$ inferred from torque magnetization and thermal conductivity. *Proc. Natl. Acad. Sci. U.S.A.* **113**, 12667–12672 (2016). doi:10.1073/pnas.1612591113 Medline

21. D. LeBoeuf, S. Krämer, W. N. Hardy, R. Liang, D. A. Bonn, C. Proust, Thermodynamic phase diagram of static charge order in underdoped $YBa_2Cu_3O_y$. *Nat. Phys.* **9**, 79–83 (2013). doi:10.1038/nphys2502

22. T. Wu, H. Mayaffre, S. Krämer, M. Horvatić, C. Berthier, W. N. Hardy, R. Liang, D. A. Bonn, M.-H. Julien, Magnetic-field-induced charge-stripe order in the high-temperature

superconductor $YBa_2Cu_3O_y$. *Nature* **477**, 191–194 (2011). doi:10.1038/nature10345 Medline

23. L. Nie, L. E. H. Sierens, R. G. Melko, S. Sachdev, S. A. Kivelson, Fluctuating orders and quenched randomness in the cuprates. *Phys. Rev. B* **92**, 174505 (2015). doi:10.1103/PhysRevB.92.174505

24. Y. Caplan, G. Wachtel, D. Orgad, Long-range order and pinning of charge-density waves in competition with superconductivity. *Phys. Rev. B* **92**, 224504 (2015). doi:10.1103/PhysRevB.92.224504

25. S. Sadewasser, J. S. Schilling, A. P. Paulikas, B. W. Veal, Pressure dependence of T c to 17 GPa with and without relaxation effects in superconducting $YBa_2Cu_3O_x$. *Phys. Rev. B* **61**, 741–749 (2000). doi:10.1103/PhysRevB.61.741

26. S. M. Souliou, H. Gretarsson, G. Garbarino, A. Bosak, J. Porras, T. Loew, B. Keimer, M. Le Tacon, Rapid suppression of the charge density wave in $YBa_2Cu_3O_{6.6}$ under hydrostatic pressure. *Phys. Rev. B* **97**, 020503 (2018). doi:10.1103/PhysRevB.97.020503

27. C. Meingast, O. Kraut, T. Wolf, H. Wühl, A. Erb, G. Müller-Vogt, Large *a*-*b* anisotropy of the expansivity anomaly at T_c in untwinned $YBa_2Cu_3O_{7-\delta}$. *Phys. Rev. Lett.* **67**, 1634–1637 (1991). doi:10.1103/PhysRevLett.67.1634 Medline

28. U. Welp, M. Grimsditch, S. Fleshler, W. Nessler, J. Downey, G. W. Crabtree, J. Guimpel, Effect of uniaxial stress on the superconducting transition in $YBa_2Cu_3O_7$. *Phys. Rev. Lett.* **69**, 2130–2133 (1992). doi:10.1103/PhysRevLett.69.2130 Medline

29. O. Kraut, C. Meingast, G. Bräuchle, H. Claus, A. Erb, G. Müller-Vogt, H. Wühl, Uniaxial pressure dependence of T_c of untwinned $YBa_2Cu_3O_x$ single crystals for x=6.5–7. *Physica C* **205**, 139–146 (1993). doi:10.1016/0921-4534(93)90180-X

30. Materials and methods are available as supplementary materials.

31. C. W. Hicks, D. O. Brodsky, E. A. Yelland, A. S. Gibbs, J. A. N. Bruin, M. E. Barber, S. D. Edkins, K. Nishimura, S. Yonezawa, Y. Maeno, A. P. Mackenzie, Strong increase of T(c) of Sr_2RuO_4 under both tensile and compressive strain. *Science* **344**, 283–285 (2014). doi:10.1126/science.1248292 Medline

32. C. W. Hicks, M. E. Barber, S. D. Edkins, D. O. Brodsky, A. P. Mackenzie, Piezoelectric-based apparatus for strain tuning. *Rev. Sci. Instrum.* **85**, 065003 (2014). doi:10.1063/1.4881611 Medline

33. A. Steppke, L. Zhao, M. E. Barber, T. Scaffidi, F. Jerzembeck, H. Rosner, A. S. Gibbs, Y. Maeno, S. H. Simon, A. P. Mackenzie, C. W. Hicks, Strong peak in T_c of Sr_2RuO_4 under uniaxial pressure. *Science* **355**, eaaf9398 (2017).

34. M. Le Tacon, A. Bosak, S. M. Souliou, G. Dellea, T. Loew, R. Heid, K.-P. Bohnen, G. Ghiringhelli, M. Krisch, B. Keimer, Inelastic x-ray scattering in $YBa_2Cu_3O_{6.6}$ reveals giant phonon anomalies and elastic central peak due to charge-density-wave formation. *Nat. Phys.* **10**, 52–58 (2014). doi:10.1038/nphys2805

35. E. M. Forgan, E. Blackburn, A. T. Holmes, A. K. R. Briffa, J. Chang, L. Bouchenoire, S. D. Brown, R. Liang, D. Bonn, W. N. Hardy, N. B. Christensen, M. V. Zimmermann, M. Hücker, S. M. Hayden, The microscopic structure of charge density waves in underdoped

$YBa_2Cu_3O_{6.54}$ revealed by x-ray diffraction. *Nat. Commun.* **6**, 10064 (2015). doi:10.1038/ncomms10064 Medline

36. K.-P. Bohnen, R. Heid, M. Krauss, Phonon dispersion and electron-phonon interaction for $YBa_2Cu_3O_7$ from first-principles calculations. *Europhys. Lett.* **64**, 104–110 (2003). doi:10.1209/epl/i2003-00143-x

37. F. Weber, S. Rosenkranz, J.-P. Castellan, R. Osborn, R. Hott, R. Heid, K.-P. Bohnen, T. Egami, A. H. Said, D. Reznik, Extended phonon collapse and the origin of the charge-density wave in ^{2}H-$NbSe_2$. *Phys. Rev. Lett.* **107**, 107403 (2011). doi:10.1103/PhysRevLett.107.107403 Medline

38. In presence of the oxygen-superstructure at this doping level (Ortho-VIII), even more phonons can be expected (36 is the number of optical modes expected for the ortho-I structure of $YBa_2Cu_3O_7$).

39. D. Reznik, L. Pintschovius, M. Ito, S. Iikubo, M. Sato, H. Goka, M. Fujita, K. Yamada, G. D. Gu, J. M. Tranquada, Electron-phonon coupling reflecting dynamic charge inhomogeneity in copper oxide superconductors. *Nature* **440**, 1170–1173 (2006). doi:10.1038/nature04704 Medline

40. D. Reznik, Phonon anomalies and dynamic stripes. *Physica C* **481**, 75–92 (2012). doi:10.1016/j.physc.2012.01.024

41. M. Raichle, D. Reznik, D. Lamago, R. Heid, Y. Li, M. Bakr, C. Ulrich, V. Hinkov, K. Hradil, C. T. Lin, B. Keimer, Highly anisotropic anomaly in the dispersion of the copper-oxygen bond-bending phonon in superconducting $YBa_2Cu_3O_7$ from inelastic neutron scattering. *Phys. Rev. Lett.* **107**, 177004 (2011). doi:10.1103/PhysRevLett.107.177004 Medline

42. L. Chaix, G. Ghiringhelli, Y. Y. Peng, M. Hashimoto, B. Moritz, K. Kummer, N. B. Brookes, Y. He, S. Chen, S. Ishida, Y. Yoshida, H. Eisaki, M. Salluzzo, L. Braicovich, Z.-X. Shen, T. P. Devereaux, W.-S. Lee, Dispersive charge density wave excitations in $Bi_2Sr_2CaCu_2O_{8+\delta}$. *Nat. Phys.* **13**, 952–956 (2017). doi:10.1038/nphys4157

43. E. Kaneshita, M. Ichioka, K. Machida, Phonon anomalies due to collective stripe modes in high T_c cuprates. *Phys. Rev. Lett.* **88**, 115501 (2002). doi:10.1103/PhysRevLett.88.115501 Medline

44. L. Pintschovius, D. Reznik, W. Reichardt, Y. Endoh, H. Hiraka, J. M. Tranquada, H. Uchiyama, T. Masui, S. Tajima, Oxygen phonon branches in $YBa_2Cu_3O_7$. *Phys. Rev. B* **69**, 214506 (2004). doi:10.1103/PhysRevB.69.214506

45. Z. P. Yin, A. Kutepov, G. Kotliar, Correlation-enhanced electron-phonon coupling: Applications of G W and screened hybrid functional to bismuthates, chloronitrides, and other high-T_c superconductors. *Phys. Rev. X* **3**, 021011 (2013). doi:10.1103/PhysRevX.3.021011

46. J. A. Robertson, S. A. Kivelson, E. Fradkin, A. C. Fang, A. Kapitulnik, Distinguishing patterns of charge order: Stripes or checkerboards. *Phys. Rev. B* **74**, 134507 (2006). doi:10.1103/PhysRevB.74.134507

47. A. Del Maestro, B. Rosenow, S. Sachdev, From stripe to checkerboard ordering of charge-density waves on the square lattice in the presence of quenched disorder. *Phys. Rev. B* **74**, 024520 (2006). doi:10.1103/PhysRevB.74.024520

48. M. Le Tacon, Uniaxial pressure control of competing orders in a high temperature superconductor. Repository KITopen (2018); doi:10.5445/IR/1000086708

49. C. T. Lin, W. Zhou, W. Y. Liang, E. Schönherr, H. Bender, Growth of large and untwinned single crystals of YBCO. *Physica C* **195**, 291–300 (1992). doi:10.1016/0921-4534(92)90353-E

50. M. Lei, J. L. Sarrao, W. M. Visscher, T. M. Bell, J. D. Thompson, A. Migliori, U. W. Welp, B. W. Veal, Elastic constants of a monocrystal of superconducting $YBa_2Cu_3O_{7-\delta}$. *Phys. Rev. B Condens. Matter* **47**, 6154–6156 (1993). doi:10.1103/PhysRevB.47.6154 Medline

51. S. G. Louie, K.-M. Ho, M. L. Cohen, Self-consistent mixed-basis approach to the electronic structure of solids. *Phys. Rev. B* **19**, 1774–1782 (1979). doi:10.1103/PhysRevB.19.1774

52. C. Elsässer, N. Takeuchi, K.-M. Ho, C. T. Chan, P. Braun, M. Fähnle, Relativistic effects on ground state properties of 4d and 5d transition metals. *J. Phys. Condens. Matter* **2**, 4371–4394 (1990). doi:10.1088/0953-8984/2/19/006

53. L. Hedin, B. I. Lundqvist, Explicit local exchange-correlation potentials. *J. Phys. C Solid State Phys.* **4**, 2064–2083 (1971). doi:10.1088/0022-3719/4/14/022

54. R. Heid, K. P. Bohnen, Linear response in a density-functional mixed-basis approach. *Phys. Rev. B* **60**, R3709–R3712 (1999). doi:10.1103/PhysRevB.60.R3709

55. E. Burkel, Phonon spectroscopy by inelastic x-ray scattering. *Rep. Prog. Phys.* **63**, 171–232 (2000). doi:10.1088/0034-4885/63/2/203